MECHANICS OF THE LEFT VENTRICLE

R. S. CHADWICK
Biomedical Engineering and Instrumentation Branch, Division of Research Services, National Institutes of Health, Bethesda, Maryland 20205

ABSTRACT A theory is presented for the mechanics of the left ventricle. A linear continuum description of the myocardium is developed, which incorporates anisotropic elastic effects due to the fiber direction field. The relation between fiber tension and fiber strain contains a time-dependent activation function that drives the ventricle around its cycle. The theory is applied to a simplified geometry consisting of a thick-walled finite cylinder in which fibers spiral on helical paths and terminate on planar end surfaces. The helix pitch angle varies continuously through the wall. The ventricular cycle is analyzed by specifying the pressures at which the aortic and mitral valves open and close. Key quantities are tabulated which permit a simple determination of the properties of the model under changes of wall thickness, fiber angles, muscle parameters, preload, afterload, etc. It is shown how the active muscle parameters can be inferred from a measurement of the end systolic pressure–volume line.

I. INTRODUCTION

The basic goal of this work is to explain the pumping action of the left ventricle of the heart in a mechanical way. It is shown how cardiac muscle fibers cooperatively act to pressurize and displace blood into the circulation in a cyclic manner. The theory is formulated as a problem in continuum mechanics in which the myocardium is represented in a way that can be interpreted as a fluid-fiber continuum.

The general linear theory developed in section II is applicable to any assumed geometrical configuration of the left ventricle. A fiber direction field is introduced to account for the fiber geometry as measured by Streeter (1979). A stress tensor is used, which was originally suggested by Peskin.[1] It incorporates the fiber direction field that gives rise to anisotropic elastic effects. The quasi-static equilibrium approximation is used at each instant of time. A linear relation between fiber stress and linearized fiber strain is used. The instantaneous elastic modulus includes a time-dependent activation function to account for the heartbeat. Strain rate or other path-dependent effects are omitted. This setting leads to a theory which is consistent with the observation of Sagawa (1978) and his co-workers that over a significant physiological range there exists an essentially linear relationship between end systolic chamber pressure and chamber volume and that this relationship is independent of preload and path. Nonlinear effects, such as finite deformation and a stress-dependent elastic modulus, are quantitatively important during diastole (Mirsky, 1979). To include such effects here would inappropriately complicate the theory at its present level of development. The intent here is to obtain a qualitative understanding and to develop some confidence that essential mechanisms are included.

In section III the theory is applied to a simplified geometry. The thick-walled finite cylinder model used previously by Feit (1979) and Arts et al. (1979) is reconsidered. In this model the fiber helix angle varies continuously through the wall, and the fibers terminate on planar end surfaces. Feit's analysis is confined to the end diastolic state which was assumed to be passive. An exponential stress-strain relation was used, and finite deformation effects were included for the case when the twisting degree of freedom was artificially suppressed. The deformation of the cylinder was calculated numerically for a prescribed chamber pressure. The calculation of Arts et al. is a simulation of the entire ventricular cycle, which was accomplished by specifying the ventricular volume as a function of time. The computation included the effect of twist and finite deformation, and used a nonlinear algebraic stress-strain relation. Time-dependent activation was not included in the calculations, which were strictly numerical from the outset. The present linear theory, when applied to the same configuration, admits a straightforward analytical solution. The displacement field includes elongation, dilation, and twist of the cylinder about its axis. The ventricular cycle is analyzed by specifying the pressures at which the aortic and mitral valves open and close. A constant chamber volume constraint is satisfied during the isovolumic contraction and isovolumic relaxation phases. Key dimensionless coefficients are tabulated that permit a simple determination of trends in the model under changes of wall thickness, fiber geometry, muscle fiber parameters, preload, afterload, etc. An important advantage of the present model is the ease with which numerical results can be obtained for different parameter values.

[1]Peskin, C. S. Unpublished notes on cardiac fiber geometry.

Section IV discusses how the results of the theory relate to experimental observations.

II. GENERAL THEORETICAL DEVELOPMENT

A Continuum Description of the Myocardium

The cardiac muscle tissue, or myocardium, is a complex interwoven structure composed primarily of cardiac muscle cells arranged in a more or less parallel weave as shown in Fig. 1. Each cell has several branches to other cells, but nonetheless a sense of direction or grain is preserved. We shall denote the local grain direction by the unit vector $\vec{\tau}$ and refer to it also as the local "fiber" direction with the understanding that individual continuous muscle fibers do not really exist. In the space external to the cells a dense capillary network is present which also runs primarily in the grain direction. Thus $\vec{\tau}$ should be relevant in any discussion of myocardial blood flow at the capillary level. From the point of view of efficient oxygen exchange between blood and cells, this parallelism is a desirable feature. It is also not difficult to imagine that the capillary blood flow is strongly dependent on the state of deformation of the cardiac cells, a fact which is well known to cardiologists. A collagen matrix that does not have a directional character also is present in the extracellular space (Borg and Caulfield, 1981). The collagen struts have a diameter of ~0.1 μm and are an order of magnitude finer than the cardiac cells and capillaries. These struts appear to be quite slack in the stress-free state. The main function of the collagen seems to be that of connecting cardiac cells to each other and to capillaries and thus of preserving the fiber directions. At large deformation the collagen no doubt is recruited and contributes to the nonlinear stiffening of the tissue.

Streeter's measurements of the direction field $\vec{\tau}$ provide a basis for constructing an anisotropic continuum theory for the myocardium. Although only $\vec{\tau}$ itself is needed in the mechanical description, it is conceptually useful to integrate the direction field and determine the fiber paths. The compact region of the left ventricle has a shape which can be roughly described as a thick-walled, truncated, prolate spheroid. In a section through the wall (Fig. 2) the projection of the direction field onto a meridional plane defines a continuum of nested closed curves. If these curves are then rotated about the axis of revolution of the spheroid, they define a system of nested toroidal surfaces. A fiber path lies on one of these toroids and winds around its surface in a helical manner. The sketch in Fig. 2 is based on a computation (Chadwick, 1981) which utilizes Streeter's measurements and assumes axial symmetry. The complexity of the fiber paths led early anatomists into the mistaken belief that the myocardium consisted of separate muscle straps, because the method of dissection went against the grain. But now it is generally agreed that the myocardium functionally behaves as a continuum (Fox and Hutchins, 1972).

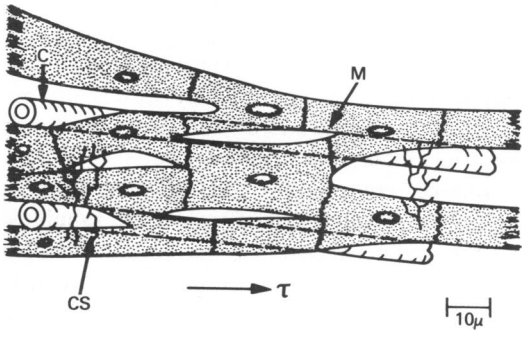

FIGURE 1 Schematic of myocardial tissue. M, myocardial cell; C, capillary; CS, collagen strut; $\vec{\tau}$ fiber direction field.

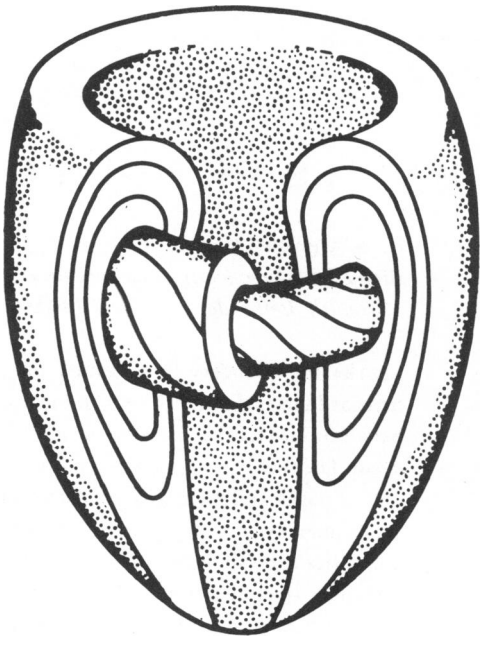

FIGURE 2 Fiber paths. Fibers spiral on toroidal shaped surfaces.

State of Stress in Myocardium

The myocardium is a complex mixture of fluid and elastic components. The fluid phase, both intracellular and extracellular, accounts for 90% of the tissue (Mirsky, 1979). There exist very general methods of continuum mechanics to deal with mixtures of fluid and solids, fluidlike solids, solidlike fluids, etc., but ultimately one has to postulate something about the nature of forces that act on material volume elements. Here we shall proceed in the more direct latter manner, and in so doing the nature of the idealizations will be clearer. Consider then the tetrahedral-shaped volume element as shown in Fig. 3, which has three orthogonal faces and a slanted

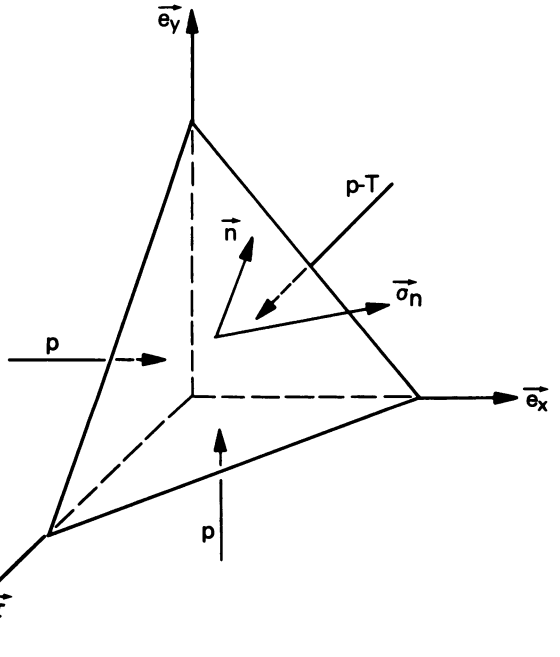

FIGURE 3 Tetrahedral-shaped volume element of tissue showing stresses acting on its surfaces.

face whose unit normal is $\vec{n}$. The element is oriented in such a way that the local fiber direction is normal to the face in the x, y plane. Because the element is mostly fluid, it is not unreasonable to postulate that a normal tissue pressure denoted by p acts on the three orthogonal faces as in any fluid at rest. In the plane of the faces we have neglected all shear stresses which could conceivably arise because of sliding action of cells and fluid, or shear of the collagen matrix. Also, no distinction is made among the pressures in different phases, such as intracellular pressure, capillary pressure, etc. Only one pressure is used here and it represents a mean value. To distinguish among these different pressures would require a much more complicated theory. The face in the x, y plane also experiences a tensile stress T due to the action of the fibers. The stress vector $\vec{\sigma}_n$ acting on the slanted face can be found by requiring the element to be in mechanical equilibrium in the limit its volume tends to zero, with the result

$$\vec{\sigma}_n = -p\vec{n} + T(\vec{\tau} \cdot \vec{n})\vec{\tau} \tag{1}$$

A stress tensor $\underset{\sim}{\sigma}$ exists having the property $\vec{\sigma}_n = \underset{\sim}{\sigma} \cdot \vec{n}$ where $\underset{\sim}{\sigma}$ is independent of $\vec{n}$. The component form is

$$\sigma_{ij} = -p\delta_{ij} + T\tau_i\tau_j \tag{2}$$

This form of the myocardial stress tensor was evidently first proposed by Peskin.[1]

Quasi-static Mechanical Equilibrium

At each instant of time the ventricular cycle is idealized as a sequence of mechanical equilibrium states, i.e., the effect of inertia will be neglected. Moskowitz (1981) has addressed this point and concluded that the difference between dynamic and quasi-static stresses is not significant for the case he analyzed, the late rapid-filling stage. If gravity and inertial forces are neglected the condition of local equilibrium is

$$\nabla \cdot \underset{\sim}{\sigma} = 0 \tag{3}$$

or

$$\nabla p = \vec{\tau}(T\nabla \cdot \vec{\tau} + \vec{\tau} \cdot \nabla T) + T(\vec{\tau} \cdot \nabla)\vec{\tau}. \tag{4}$$

This gives the relation between the pressure gradient, the tension, and the fiber direction fields. As Peskin (1975) has pointed out, the pressure gradient vector locally lies in what is called the osculating plane of fiber, which is the plane determined by the local tangent vector and principal normal vector of the fiber. The vector $(\vec{\tau} \cdot \nabla)\vec{\tau}$ is the rate of change of the fiber tangent vector with respect to the arc length along the fiber, and is the principal normal. Eq. 4 states that in general a pressure gradient can exist in a direction tangent to a fiber if there is either a tension gradient along the fiber or the fiber direction field has a nonzero divergence. Also if the fibers have a curvature, then a component of the pressure gradient lies along the principal normal. This latter situation has often been applied in various forms to the mechanical analysis of the heart wall and has been referred to as the law of Laplace in the physiology literature.

Fiber Strain

In addition to the pressure and tension fields that specify the state of stress we also introduce the displacement vector $\vec{u}$ which specifies the state of deformation. $\vec{u}$ is measured relative to some reference configuration free of stress. Since the myocardium is essentially incompressible, any arbitrary volume element must deform in such a way that its volume remains unchanged. This neglects the effect of changing myocardial blood volume. The linearized tissue incompressibility constraint is then given by

$$\nabla \cdot \vec{u} = 0. \tag{5}$$

A quantity of importance in the theory to be developed is the linearized fiber strain which will be denoted by ϵ. Let ds_0 and ds be the infinitesimal distances between two neighboring points on a fiber in the unstrained and strained states, respectively. Then ϵ is defined by

$$\epsilon = \lim_{ds_0 \to 0} \frac{ds - ds_0}{ds_0} \tag{6}$$

i.e., the fractional change of length of a fiber. In terms of $\vec{u}$ and $\vec{\tau}$, this limit works out to be

$$\epsilon = [(\vec{\tau} \cdot \nabla)\vec{u}] \cdot \vec{\tau} \tag{7}$$

Note that in this linearized theory $\vec{\tau}$ is the unstrained direction field and is a known quantity.

Relationship between Tension, Fiber Strain, and Activation

Sagawa (1978) has reviewed experimental studies pertaining to both the pressure-volume relation of the intact ventricle and the length-tension relation of isolated papillary muscle. The intact ventricle actually has the simpler behavior in that the pressure-volume relation shows no significant path or rate dependence over a wide physiological range. If we suppose that intact myocardial fibers have this same property then fiber stress can be related to fiber strain independent of stress or strain history. However, a complicating feature is the degree of activation of the fibers. As a guide, consider the behavior of isometric contractions of papillary muscle. If the tension is recorded at fixed length as a function of time, and this is repeated at different muscle lengths, then a family of curves of tension vs. strain can be obtained with time as a parameter. Two such curves are sketched in Fig. 4. The lower curve represents the passive state and has a linear region characterized by a passive modulus E. The upper curve is he locus of tension at maximal activation vs. strain. It also has a significant linear region whose slope E^* is an active modulus, with $E^* > E$. The intercept T_0 is the maximal isometric tension at zero strain. Thus, for the linear regions

$$T = \begin{cases} E\epsilon & \text{passive state} \quad (8a) \\ E^*\epsilon + T_0 & \text{maximally active state} \quad (8b) \end{cases}$$

The tension-strain relation at intermediate times (or degree of activation) is also essentially linear (Brady, 1979). The entire family of tension vs. strain relations can be represented by a linear combination of Eqs. 8a and 8b by introducing an activation function $\beta(t)$.

$$T = [(1 - \beta)E + \beta E^*)]\epsilon + \beta T_0. \tag{8c}$$

In the ventricle $\beta(t)$ is a dimensionless periodic function of time (determining the heartbeat) oscillating between zero and unity. Note than when $\beta = 0$ and $\beta = 1$, Eqs. 8a and 8b are recovered, respectively. To account for nonsimultaneous activation of all fibers, the activation function can be made to depend also on the spatial coordinates. Nonhomogeneity of the

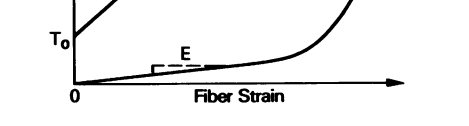

FIGURE 4 Tension-strain behavior of cardiac muscle.

myocardium, if it exists, could be accounted for by allowing E, E^*, and T_0 to depend on the spatial coordinates.

Eq. 8c has a simple interpretation at the sarcomere level. It states that a passive linear spring (e.g., the sarcolemma) is in parallel with an active tension generator (the contractile proteins). In cardiac muscle, opposing actin filaments overlap each other. If either the cross-bridges cannot attach in these regions of opposing actin overlap or cross-bridges can attach equally likely to actin filaments attached to opposite ends of the sarcomere, then these regions do not contribute to active tension generation. If we assume that the active tension is proportional to the length of actin-myosin overlap excluding the overlap of opposing actins, then we obtain a stress-strain law having the same form as Eq. 8c. In other words, the linear decrease of opposing actin overlap with increasing sarcomere length accounts for the linear increase in active tension with increasing strain. The overlap length of interdigitating actin filaments is ~0.15 μm at the resting (zero passive strain) sarcomere length of ~1.90 μm. A linear increase in active tension can be expected until there is no opposing actin overlap, i.e., for strains $\epsilon \sim 0.15/1.90$, which is ~8%. This figure agrees with what is found experimentally (Braunwald et al., 1976, p. 82).

Left Ventricular Cycle

The beating ventricle goes through a sequence of mechanical changes that are conveniently represented on a chamber pressure–chamber volume diagram as shown in Fig. 5. Point 0 is the reference state from which all other states are measured. It is the strain-free state defined by the chamber volume V_0 which exists at zero chamber pressure. Pressure is measured relative to the pressure acting on the outside surface of the ventricular free wall. Also the pressure is assumed to be uniform inside the chamber. A normal physiological loop consists of the counterclockwise sequence 4-1-2-3-4 with the leg 2-3 along the dotted path. Other types of loops can be made to occur in the laboratory (see Sagawa, 1978, for a review). The leg 2-3 along the solid path is an isobaric ejection which occurs when the ventricle ejects into a constant pressure reservoir. If ejection is prevented either by clamping the aorta or preventing the aortic valve from opening by use of an occluding balloon, then the ventricle contracts isovolumically and cycles between points 1 and 2′. The normal physiological loop consists of four distinct legs: diastolic filling 4-1 (open mitral valve, closed aortic valve); isovolumic contraction 1-2 (both valves closed); systolic ejection 2-3 (open aortic valve, closed mitral valve); and isovolumic relaxation 3-4 (both valves closed). The "corners" of the loop, i.e., the points 1, 2, 3, and 4, are characterized by the opening and closing of the two valves. These points are quite well defined if the valves are functioning normally. The activation parameter $\beta(t)$ would be falling toward zero during isovolumic relaxation and diastolic filling, and rising toward unity during isovolumic contraction and systolic ejection.

Several important ventricular performance indices are available from the pressure-volume loop. The stroke work is the area enclosed by the loop. The stroke volume is the quantity of blood ejected by the ventricle $V_1 - V_3$. Ejection fraction is the normalized stroke volume, $(V_1 - V_3)/V_1$. Also, the end systolic pressure-volume relation as indicated by the line 5-3-2′ in Fig. 5 has been experimentally studied by Sagawa and his co-workers. Its slope and intercept V_d are thought to be indicators of the inherent contractility of the ventricle. We will show, in fact, that the active muscle parameters E^* and T_0 determine the locus of end systolic states.

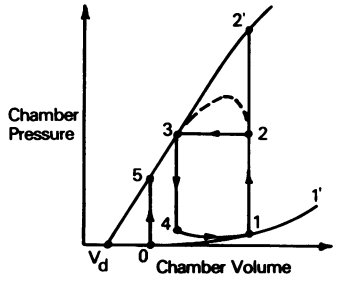

FIGURE 5 Ventricular pressure-volume diagram.

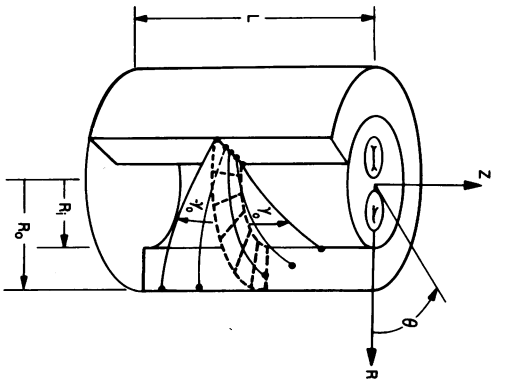

FIGURE 6 Finite thick-walled cylindrical model of left ventricle. Fibers are on cylindrical surfaces and helix angle varies continuously through the wall.

III. APPLICATION TO A THICK-WALLED FINITE CYLINDER MODEL

For this configuration, as shown in Fig. 6, the analysis is straightforward and an explicit analytical solution can be found. The cylinder has length L, inner radius R_i, and outer radius R_0. The upper surface ($z = 0$) is assumed to be fixed. On this surface radial displacements are allowed, but axial and circumferential displacements are zero. The bottom surface ($z = -L$) is assumed to be a free plane which can translate vertically and twist as a rigid body about the axis of the cylinder. Radial displacements are allowed to occur to maintain the cylindrical shape. The parameters of the model are summarized in Table I.

The fiber direction field will be taken to be

TABLE I
VENTRICULAR PARAMETERS

Reference geometry		Fiber characteristics		Opening and closing pressures of valves	
R_i	inside radius	E	passive elastic modulus (dyne/cm^2)	$p_1(R_i)$	Mitral Closes
R_o	outside radius	E^*	maximally active elastic modulus (dyne/cm^2)	$p_2(R_i)$	Aortic Opens
L_o	length	T_o	maximum active tension generated at zero strain (dyne/cm^2)	$p_3(R_i)$	Aortic Closes
γ_o	maximum fiber helix angle	β	activation function (dimensionless)	$p_4(R_i)$	Mitral Opens
$\alpha = R_o/R_i$					

$$\vec{\tau} = \cos\gamma\,(R)\vec{e}_\theta + \sin\gamma\,(R)\vec{e}_z. \qquad (9)$$

Thus, the fibers form regular helices on cylindrical surfaces. The axial pitch angle $\gamma(R)$ varies continuously across the wall of the cylinder. A small radial component of the direction field has been neglected in Eq. 9 which makes the helices wind on the toroids sketched in Fig. 2.

Axisymmetric Solution

Eqs. 4, 5, and 7 can be written in cylindrical coordinates (see Chadwick, 1981) using Eq. 9 as the fiber direction field. When all theta derivatives vanish it follows that pressure, tension, and fiber strain fields are functions of time and the radial coordinate only. The displacement field $\vec{u}$ with components (u_R, u_θ, u_Z) has the form

$$\begin{aligned} u_R &= -\tfrac{1}{2}C_1(t)R + C_2(t)/R \\ u_\theta &= -zR\theta_0(t)/L \\ u_Z &= C_1(t)z \end{aligned} \qquad (10)$$

with $C_1(t)$, $C_2(t)$, $\theta_0(t)$ arbitrary functions of time. $C_1(t)$ is the axial strain, $\theta_0(t)$ is the twist angle of the bottom plane, and $C_2(t)$ is related to ventricular compliance. The tension field is given by Eq. 8c where the fiber strain is

$$\epsilon(R,t) = C_1(t)\left[1 - \frac{3}{2}\cos^2\gamma\,(R)\right] + \frac{C_2(t)}{R^2}\cos^2\gamma\,(R) - \frac{\theta_0(t)R}{L}\sin\gamma\,(R)\cos\gamma\,(R) \qquad (11)$$

The pressure field is obtained from the tension field by

$$p(R,t) = \int_R^{R_o} T(r,t)\cos^2\gamma\,(r)\frac{dr}{r} \qquad (12)$$

which satisfies the condition that the pressure vanish on the outside radius of the cylinder. Three further conditions of constraint are needed to determine the three arbitrary functions of time. The bottom plane must be in vertical force equilibrium, which leads to

$$\int_{R_i}^{R_o} T(R,t)\,[\,2\sin^2\gamma\,(R) - \cos^2\gamma(R)\,]\,R\,dR = 0. \qquad (13)$$

Also, the bottom plane must be in moment equilibrium about the cylinder axis, which gives

$$\int_{R_i}^{R_o} T(R,t)\sin\gamma\,(R)\cos\gamma\,(R)R^2\,dR = 0. \qquad (14)$$

The remaining condition is more subtle and depends on how the boundary conditions are specified during the course of the cycle. The difficulty is due to the fact that during ejection 2-3 the ventricle is coupled mechanically to the aorta and during filling 4-1 the atrium and ventricle are coupled. To actually include these coupling effects, which would have to also include the mechanics of valve opening and closure, greatly complicates the theory and calculation, and will not be dealt with here. Arts et al. (1979) avoided the problem by specifying the chamber volume as a function of time. If the same procedure were to be followed here, it would be equivalent to specifying $C_2(t)$, because $V(t) = V_0\,(1 + 2C_2(t)/R_i^2)$ to an accuracy consistent with linear theory. Then Eqs. 13 and 14 are sufficient to determine $C_1(t)$ and $\theta_0(t)$, and hence the entire solution. However, another approach has been taken here that is aimed at determining the mechanical state of the ventricle at the four corner points of the p-V loop of Fig. 5. At state 1, end diastole, the activation function β is assumed to be zero, and the preload pressure $p_1(R_i)$ is specified. Then Eq. 12, evaluated at $R = R_i$, provides the additional equation for the determination of C_1, C_2, θ_0. The solution to the resulting system of three linear algebraic equations is given in Tables II, III, and IV, where $C_{11} = C_1$, $C_{12} = C_2/R_i^2$, and

TABLE II
$C_{11}/(P_1/E)$

	γ_o								
α	50°	55°	60°	65°	70°	75°	80°	85°	90°
1.1	58.304	36.332	23.598	16.047	11.499	8.729	7.023	5.950	5.245
1.2	30.070	18.834	12.274	8.364	6.002	4.560	3.670	3.110	2.741
1.3	20.489	12.927	8.466	5.787	4.161	3.164	2.548	2.160	1.904
1.4	15.594	9.926	6.539	4.487	3.234	2.463	1.985	1.683	1.484
1.5	12.590	8.093	5.366	3.698	2.673	2.039	1.645	1.396	1.230
1.6	10.542	6.847	4.572	3.166	2.294	1.754	1.417	1.202	1.060
1.7	9.050	5.939	3.995	2.780	2.021	1.548	1.252	1.063	0.937
1.8	7.909	5.246	3.555	2.486	1.813	1.392	1.127	0.958	0.845
1.9	7.007	4.696	3.206	2.253	1.649	1.268	1.029	0.875	0.772
2.0	6.276	4.249	2.922	2.064	1.516	1.168	0.949	0.808	0.713

TABLE III
$C_{12}/(P_1/E)$

	γ_o								
α	50°	55°	60°	65°	70°	75°	80°	85°	90°
1.1	36.306	29.520	26.709	25.987	26.384	27.386	28.714	30.213	31.799
1.2	20.551	16.791	15.234	14.846	15.089	15.674	16.443	17.310	18.225
1.3	15.305	12.593	11.470	11.205	11.406	11.862	12.455	13.121	13.822
1.4	12.685	10.525	9.634	9.439	9.627	10.026	10.539	11.112	11.714
1.5	11.114	9.308	8.568	8.422	8.610	8.981	9.453	9.977	10.526
1.6	10.067	8.517	7.886	7.781	7.973	8.333	8.783	9.280	9.800
1.7	9.321	7.967	7.423	7.353	7.555	7.911	8.351	8.835	9.339
1.8	8.764	7.568	7.097	7.059	7.274	7.632	8.070	8.548	9.045
1.9	8.332	7.270	6.862	6.854	7.083	7.449	7.889	8.367	8.863
2.0	7.989	7.042	6.691	6.711	6.956	7.332	7.779	8.262	8.761

TABLE IV
$C_{13}/(P_1/E)$

	γ_o								
α	50°	55°	60°	65°	70°	75°	80°	85°	90°
1.1	−0.293	−0.560	−0.585	−0.532	−0.464	−0.403	−0.351	−0.307	−0.264
1.2	−0.273	−0.525	−0.550	−0.501	−0.438	−0.381	−0.333	−0.291	−0.251
1.3	−0.252	−0.488	−0.514	−0.471	−0.412	−0.359	−0.314	−0.275	−0.237
1.4	−0.231	−0.452	−0.479	−0.441	−0.387	−0.338	−0.296	−0.260	−0.224
1.5	−0.211	−0.417	−0.446	−0.412	−0.363	−0.318	−0.279	−0.246	−0.212
1.6	−0.192	−0.384	−0.414	−0.385	−0.341	−0.299	−0.264	−0.232	−0.201
1.7	−0.175	−0.354	−0.384	−0.359	−0.319	−0.281	−0.248	−0.219	−0.190
1.8	−0.159	−0.326	−0.357	−0.335	−0.300	−0.265	−0.234	−0.207	−0.180
1.9	−0.145	−0.300	−0.331	−0.313	−0.281	−0.249	−0.221	−0.196	−0.170
2.0	−0.132	−0.276	−0.308	−0.293	−0.264	−0.235	−0.209	−0.186	−0.161

$C_{13} = \theta_0 R_i/L$. The computations are carried out for a linear distribution of fiber helix angles

$$\gamma(\rho; \gamma_0, \alpha) = \frac{\gamma_0}{\alpha - 1}(1 + \alpha - 2\rho) \qquad 1 \le \rho \le \alpha$$

$$\rho = R/R_i; \qquad \alpha = R_o/R_i \tag{15}$$

so that $\gamma = \gamma_0$ on the inside surface, $\gamma = -\gamma_0$ on the outside surface, and $\gamma = 0$ at midwall (Fig. 6). The coefficients are tabulated as functions of the ventricular geometry as specified by γ_0, α.

The remaining corners of the cycle can be expressed as linear combinations of the end diastolic state 1 and an auxiliary state 5 (Fig. 5) which is clamped isovolumic contraction from zero preload. This state lies on the end systolic pressure–volume line which is assumed to characterize states with activation parameter β set at unity (see Discussion for further significance of state 5). The isovolumic constraint implies $C_2 = 0$ for state 5. Then Eqs. 13 and 14 result in two linear algebraic equations for the determination of C_1 and θ_0. Tables V, VI, and VII give C_{51}, C_{53}, and $p_5(R_i)$ as functions of γ_0 and α, where $C_{51} = C_1$ and $C_{53} = \theta_0 R_i/L$ for state 5.

To determine state 2, the end of isovolumic contraction, we specify $p_2(R_i)$ which is the aortic diastolic pressure or the pressure at which the aortic valve opens. However, there is also the isovolumic constraint so that $C_2 = 0$ for state 2 relative to state 1. Eqs. 13 and 14 then determine the constants. Eq. 12 evaluated at $R = R_i$ then determines the value of β which is consistent with the specified $p_2(R_i)$. In other words, specifying the chamber pressure at the instant of aortic valve opening determines the value of the activation parameter. State 2 is given by relations

$$\vec{u}_2 = \vec{u}_1 + \frac{\beta E^*}{\beta E^* + (1 - \beta)E}\vec{u}_5 \tag{16}$$

$$T_2 = \beta T_5 + \left[1 + \left(\frac{E^* - E}{E}\right)\beta\right] T_1 \tag{17}$$

$$p_2(R) = \beta p_5(R) + \left[1 + \left(\frac{E^* - E}{E}\right)\beta\right] p_1(R) \tag{18}$$

TABLE V
$C_{51}/(T_0/E^*)$

	γ^0								
α	50°	55°	60°	65°	70°	75°	80°	85°	90°
1.1	1.657	1.038	0.465	0.025	−0.276	−0.470	−0.593	−0.672	−0.726
1.2	1.660	1.047	0.477	0.037	−0.265	−0.461	−0.586	−0.667	−0.721
1.3	1.664	1.059	0.494	0.055	−0.249	−0.448	−0.575	−0.659	−0.715
1.4	1.668	1.074	0.514	0.076	−0.230	−0.432	−0.563	−0.649	−0.708
1.5	1.674	1.091	0.537	0.100	−0.208	−0.414	−0.548	−0.638	−0.700
1.6	1.679	1.108	0.561	0.125	−0.186	−0.395	−0.533	−0.626	−0.691
1.7	1.685	1.125	0.586	0.151	−0.162	−0.375	−0.517	−0.613	−0.681
1.8	1.690	1.143	0.610	0.177	−0.138	−0.355	−0.501	−0.601	−0.672
1.9	1.696	1.160	0.635	0.203	−0.115	−0.335	−0.484	−0.588	−0.662
2.0	1.701	1.176	0.658	0.228	−0.091	−0.314	−0.468	−0.575	−0.652

TABLE VI
$C_{53}/(T_0/E^*)$

	γ_0								
α	50°	55°	60°	65°	70°	75°	80°	85°	90°
1.1	−0.148	−0.150	−0.142	−0.129	−0.116	−0.104	−0.094	−0.086	−0.079
1.2	−0.266	−0.271	−0.258	−0.234	−0.210	−0.188	−0.170	−0.156	−0.143
1.3	−0.361	−0.368	−0.350	−0.319	−0.287	−0.257	−0.233	−0.213	−0.196
1.4	−0.435	−0.445	−0.424	−0.388	−0.349	−0.314	−0.284	−0.260	−0.238
1.5	−0.492	−0.504	−0.482	−0.442	−0.399	−0.359	−0.326	−0.298	−0.273
1.6	−0.536	−0.550	−0.528	−0.486	−0.439	−0.396	−0.359	−0.329	−0.302
1.7	−0.568	−0.585	−0.563	−0.520	−0.471	−0.426	−0.387	−0.354	−0.325
1.8	−0.592	−0.611	−0.590	−0.546	−0.496	−0.449	−0.409	−0.374	−0.343
1.9	−0.608	−0.629	−0.610	−0.566	−0.516	−0.468	−0.426	−0.390	−0.358
2.0	−0.619	−0.642	−0.624	−0.581	−0.531	−0.482	−0.440	−0.403	−0.369

where

$$\beta = \frac{p_2(R_i) - p_1(R_i)}{p_5(R_i) + \left(\frac{E^* - E}{E}\right)p_1(R_i)}. \tag{19}$$

Eq. 19 has a simple physical interpretation. It states that the value of the activation parameter at the time of aortic valve opening is the ratio of the difference between aortic diastolic pressure and preload pressure and the difference between the clamped end isovolumic pressure ($p_{2'}$) and preload pressure.

State 3, the end of ejection, is on the end systolic pressure–volume line ($\beta = 1$) and is given by

$$\vec{u}_3 = \vec{u}_5 + \left[\frac{p_3(R_i) - p_5(R_i)}{p_1(R_i)}\right]\frac{E}{E^*}\vec{u}_1 \tag{20}$$

$$T_3 = T_5 + \left[\frac{p_3(R_i) - p_5(R_i)}{p_1(R_i)}\right] T_1 \tag{21}$$

$$p_3(R) = p_5(R) + \left[\frac{p_3(R_i) - p_5(R_i)}{p_1(R_1)}\right] p_1(R) \tag{22}$$

where $p_3(R_i)$ is the specified chamber pressure at aortic valve closure.

State 4, the end of isovolumic relaxation, is determined by specifying $p_4(R_i)$, the pressure at which the mitral valve opens. However, there is also the isovolumic constraint so that $C_2 = 0$ for state 4 relative to state 3. Again Eqs. 13 and

TABLE VII
$P_5(R_i)/T_0$

	γ_0								
α	50°	55°	60°	65°	70°	75°	80°	85°	90°
1.1	0.045	0.056	0.062	0.063	0.063	0.060	0.058	0.055	0.052
1.2	0.087	0.106	0.118	0.121	0.119	0.115	0.110	0.104	0.992
1.3	0.125	0.153	0.169	0.174	0.171	0.165	0.157	0.150	0.142
1.4	0.160	0.195	0.215	0.222	0.219	0.211	0.201	0.191	0.182
1.5	0.192	0.234	0.253	0.266	0.262	0.253	0.241	0.230	0.218
1.6	0.223	0.270	0.298	0.306	0.302	0.292	0.279	0.265	0.252
1.7	0.252	0.304	0.334	0.344	0.339	0.328	0.313	0.298	0.283
1.8	0.279	0.335	0.368	0.379	0.374	0.361	0.345	0.328	0.312
1.9	0.304	0.365	0.400	0.411	0.406	0.392	0.375	0.357	0.339
2.0	0.328	0.392	0.430	0.442	0.436	0.421	0.403	0.383	0.364

14 determine the constants, and Eq. 12 determines β. State 4 is given by

$$\vec{u}_4 = \frac{\beta E^*}{\beta E^* + (1-\beta)E}\vec{u}_5 + \left[\frac{p_3(R_i) - p_5(R_i)}{p_1(R_i)}\right]\frac{E}{E^*}\vec{u}_1 \quad (23)$$

$$T_4 = \beta T_5 + \left[\frac{E}{E^*}(1-\beta) + \beta\right]\left[\frac{p_3(R_i) - p_5(R_i)}{p_1(R_i)}\right]T_1 \quad (24)$$

$$p_4(R) = \beta p_5(R) + \left[\frac{E}{E^*}(1-\beta) + \beta\right] \cdot \left[\frac{p_3(R_i) - p_5(R_i)}{p_1(R_i)}\right]p_1(R) \quad (25)$$

where

$$\beta = \frac{p_4(R_i) - \frac{E}{E^*}[p_3(R_i) - p_5(R_i)]}{p_3(R_i) - \frac{E}{E^*}[p_3(R_i) - p_5(R_i)]}. \quad (26)$$

Note that at state 4 $\beta > 0$, in general, so the filling process 4-1 is not passive. This is consistent with the observation that ventricular pressure is falling while ventricular volume is increasing during the rapid-filling phase.

Numerical Results

Results are summarized in Table VIII for the following example: $R_i = 1$ cm, $L_0 = 4.77$ cm, $\alpha = 1.6$, $\gamma_0 = 70°$, $V_0 = 15$ ml, $E = 3 \times 10^5$ dyn/cm^2, $E^* = 22.3 \times 10^5$ dyn/cm^2, $T_0 = 2.5 \times 10^5$ dyn/cm^2, $p_1 = 10$ mmHg, $p_2 = 80$ mmHg, $p_3 = 85$ mmHg, and $p_4 = 15$ mmHg. These parameters are thought to be representative for the canine left ventricle. The symbols used in the table are $\Delta L/L_0$ = axial strain, $\Delta H/H_0$ = fractional increase in wall thickness, $\Delta R/R_0$ = fractional increase in outside radius, θ_0 = twist angle of lower plane, β = activation parameter, and V = ventricular volume. All of the entries in Table VIII can easily be obtained by use of only a pocket calculator and Tables II–VII.

The distribution of fiber strain and sarcomere length

TABLE VIII
GEOMETRICAL AND ACTIVATION CHANGES IN EXAMPLE CALCULATION

	State			
	1	2	3	4
$\%\Delta L/L_0$	10.20	8.29	1.81	2.76
$\%\Delta H/H_0$	−27.25	−26.30	− 9.36	− 9.84
$\%\Delta R/R_0$	17.05	18.00	7.55	7.08
θ_0, degrees	− 4.14	−16.42	−15.03	− 8.89
β	0	0.579	1	0.138
V, milliliters	25.6	25.6	19.0	19.0

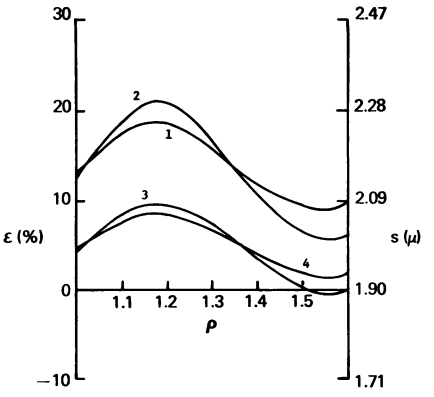

FIGURE 7 Distribution of fiber strain and sarcomere length through ventricular wall for the different equilibrium states. ($\rho = R/R_i$).

across the wall is shown in Fig. 7 for the same example. The relationship between the two quantities is $\epsilon = (s - s_0)/s_0$ where s is the sarcomere length in the strained state and s_0 is the unstrained length which is taken to be 1.9 μm uniformly throughout the wall. Note that the sarcomere length is maximal in the subendocardial layer throughout the cycle. The corresponding tension and pressure distributions are shown in Fig. 8 and Fig. 9.

Ejection fraction is plotted in Fig. 10 as a function of dimensionless preload pressure p_1/E and a dimensionless parameter $\zeta = (p_5 - p_3)/E^*$. The parameter is a combination of afterload pressure p_3 and the active muscle parameters T_0 and E^*. For fixed α and γ_0, the ejection fraction as a function of preload and afterload pressures, and active and passive muscle parameters, collapses onto a single surface

$$EF = f(p_1/E, \zeta).$$

It is apparent from Fig. 10 that the ejection fraction is a monotonic, increasing function of its arguments, at least for the plotted range of physiological interest. Thus the ejection fraction increases with increasing preload pressure (a demonstration of Starling's law), increasing active tension at zero strain, or decreasing passive stiffness, decreasing afterload pressure and decreasing active stiffness provided $p_5 > p_3$. If $p_5 < p_3$ then decreasing the active stiffness decreases the ejection fraction. Changing the

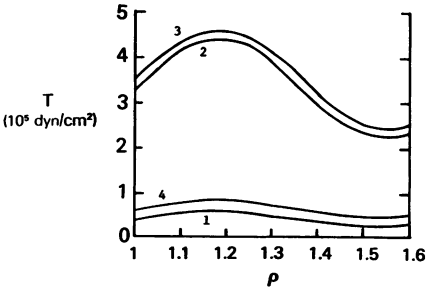

FIGURE 8 Distribution of fiber tension through ventricular wall for the different equilibrium states.

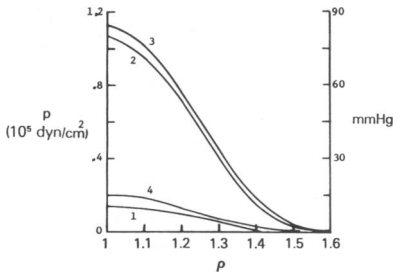

FIGURE 9 Distribution of tissue pressure through ventricular wall for the different equilibrium states.

geometrical parameters α and γ_0 results in a different ejection fraction surface. For example, with an increase in α as in hypertrophy the surface lies under the surface for smaller α. Therefore for fixed p_1/E and ζ an increase in α results in a lower ejection fraction. However, an increase in α increases p_5 so that ζ increases even if T_0, p_3, and E^* are fixed, and this increase in ζ is enough to increase the ejection fraction.

Calculated pressure-volume loops are shown in Fig. 11 at different preload and afterload pressures for the case of isobaric ejection. Values of the geometrical and muscle parameters are the same as used previously.

IV. DISCUSSION

It is interesting to examine some of the effects due to variation in the maximum helix angle parameter γ_0. It is apparent from Table VII that p_5 is maximized when γ_0 is ~65°, i.e., the cylinder has the maximal capability to generate pressure in a clamped isovolumic contraction at this helix angle. Streeter's measurements show that this angle is observed in canine ventricles. The theory may also resolve a controversy concerning the normal geometrical changes during isovolumic contraction. Both lengthening of the external major axis with shortening of the external minor diameter (isovolumic ellipticalization) and short-

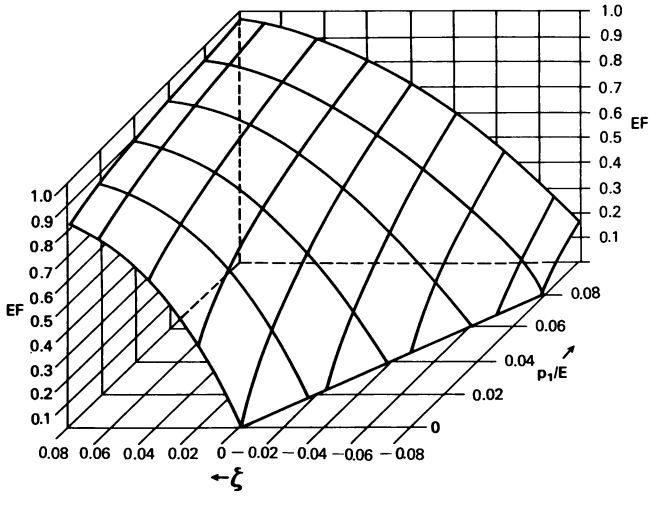

FIGURE 10 Ejection fraction surface. $\zeta = (p_5 - p_3)/E^*$.

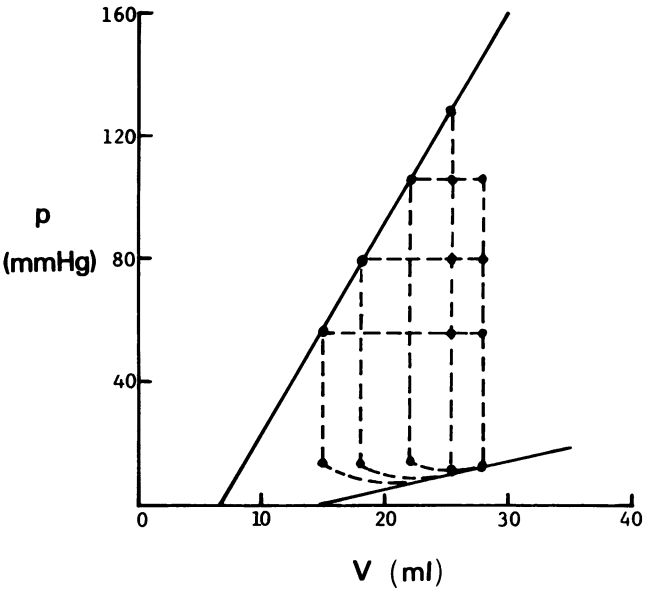

FIGURE 11 Calculated pressure-volume loops for isobaric ejection from different preload and afterload pressures.

ening of the external major axis with lengthening of the external minor diameter (isovolumic sphericalization) have been observed experimentally (Rankin et al., 1976). In terms of the notation of the present paper, the former would occur if $C_{51} > 0$ and the latter would occur if $C_{51} < 0$. Referring to Table V, we can see that C_{51} changes sign if $65° < \gamma_0 < 70°$, which is within the normal physiological range for canine ventricles. Thus normal variation between different animals could account for the different observations. Rankin et al. also found that both patterns could be observed in the same dog depending on the end diastolic volume. That could represent the nonlinear effect of a changing fiber direction field with large diastolic deformations.

There are some experimental observations that tend to validate the basic ideas of the theory and specifically some of the predictions from the cylindrical model. I have observed a twist of the apex relative to the base of a beating canine ventricle with the correct sense of rotation and magnitude estimated to be about 10°–20°. The distribution of sarcomere length across the wall as shown in Fig. 7 indicates that throughout the cycle the longest sarcomeres are in the subendocardial layers. Measurements of Yoran et al. (1973) at end diastole substantiate this prediction. In the calculations of Arts et al. it was assumed that the sarcomere length distribution is uniform at end diastole instead of being uniform in the stress-free reference state as was assumed here and also by Feit.

Fig. 9 predicts a smooth decrease in tissue pressure varying between ventricular chamber pressure on the inside surface and zero pressure on the outside surface, which are the assumed boundary conditions. This trend is consistent throughout the ventricular cycle. For the cylindrical model, tissue pressure is equivalent to the negative of

radial stress for the case of zero radial component of the fiber direction field (Eq. 1). These results are in qualitative agreement with predictions of the other fiber-based cylindrical models. Unfortunately, attempts to measure the tissue pressure have not led to any consistent results. Pierce (1981) has reviewed the various methods used to measure tissue pressure. The techniques that are used tend to cause local edema and contractile dysfunction which would disturb the measurement. In any case, some of the measurements qualitatively agree with the present theory while others do not. For example, some measurements indicate that tissue pressure can exceed the chamber pressure and that a substantial positive pressure gradient can exist from endocardium to epicardium. To resolve this problem, several issues must be considered. To begin with, the concept of tissue pressure is itself an idealization in that no distinction is made among pressures in the different phases. Nontraumatic measurement techniques must be found and the stress component actually being measured must be identified.

Sagawa (1978) has found that the end systolic chamber pressure and volume experimentally satisfy to a good approximation the empirical linear relationship

$$p_{ES} = E_{ES}(V_{ES} - V_d) \tag{27}$$

where E_{ES} is the constant slope (a volume elastance) of the end systolic pressure-volume line, V_d is a "correction volume," and $p_{ES} = p_3$, $V_{ES} = V_3$ in our notation. The same relationship is predicted by our theory with

$$E_{ES} = \frac{1}{2}\frac{E^*}{\tilde{C}_{12}V_0} \tag{28}$$

$$V_d = V_0\left(1 - 2\tilde{C}_{12}\tilde{p}_5\frac{T_0}{E^*}\right) = V_0 - p_5/E_{ES} \tag{29}$$

where $\tilde{C}_{12} = C_{12}/(p_1/E)$ is tabulated in Table III, and $\tilde{p}_5 = p_5(R_i)/T_0$ is in Table VII. Thus an experimental measurement of E_{ES} and V_d would determine the two active muscle parameters E^* and T_0. The fact that Eq. 27 is linear and that it is independent of preload and path supports the basic assumptions of theory. Namely, in the beating heart it is appropriate to consider a linear quasi-static equilibrium theory without significant dissipative effects. The linearity of Eq. 27 breaks down at large diastolic volumes as one would expect on the basis of finite deformation effects. Eqs. 28 and 29 provide a means of explaining many of Sagawa's observations as well as giving more insight into his findings. A positive inotropic intervention increases E_{ES}, which implies an increase in E^* because the denominator of Eq. 28 is a function only of the reference geometry. Sagawa realized that E_{ES} itself is not a true indicator of inherent contractility because different sized hearts would have different E_{ES} even with the same contractile state. It is E^* and not E_{ES} that is a contractility index and Eq. 28 shows how to normalize E_{ES} to account for size. Sagawa also observed that the "correction volume" V_d is always less than the stress-free reference volume V_0. This is borne out by Eq. 29, which also indicates how V_d is a measure of $p_5(R_i)$, the clamped isovolumic chamber pressure at zero preload. Sagawa further observed that V_d is insensitive to inotropic intervention which indicates that the ratio T_0/E^* remains rather constant. Ventricular hypertrophy (an increase in α) under conditions of fixed V_0, E^*, and T_0 would have the effect of increasing E_{ES} and decreasing V_d since $\tilde{C}_{12}$ is a decreasing function of α and the product $\tilde{C}_{12}\tilde{p}_5$ is an increasing function of α (see Tables III and VII).

In Fig. 11 the calculated E_{ES} is 7.0 mmHg/ml which is typical of values reported by Sagawa for the canine ventricle. Also, the values of the active muscle parameters which were used to determine E_{ES} are typical of reported values for the canine papillary muscle. Therefore, there exists an internal consistency among different physiological measurements and properties of the model.

The author is grateful for the encouragement of and many useful discussions with Dr. Seth Goldstein and Dr. Allen Waxman of the Biomedical Engineering and Instrumentation Branch, Division of Research Services, National Institutes of Health; Dr. Randolph Patterson of the Cardiology Branch, National Heart, Lung and Blood Institute; Professor Charles Peskin of the Courant Institute of Mathematical Sciences; Professor Robert Mates of the Department of Mechanical and Aeronautical Engineering, The State University of New York at Buffalo; Professor J. D. Cole of the Mechanics and Structures Department, University of California, Los Angeles; and especially Harriette Jordan for her typing and editorial assistance.

Received for publication 21 October 1981 and 8 February 1982.

REFERENCES

Arts, T., R. S. Reneman, and P. C. Veenstra. 1979. A model of the mechanics of the left ventricle. *Ann. Biomed. Eng.* 7:299–318.

Brady, A. J. 1979. Mechanical properties of cardiac fibers. *In* Handbook of Physiology Vol. 1. R. M. Berne, N. Sperelakis, and S. R. Geiger, editors. American Physiological Society, Bethesda, Maryland. Section 2.

Borg, T. K., and J. B. Caulfield. 1981. The collagen matrix of the heart. *Fed. Proc.* 40:2037–2041.

Braunwald, E., J. Ross, and E. H. Sonnenblick. 1976. Mechanisms of Contraction of the Normal and Failing Heart. Little, Brown and Company, Boston.

Chadwick, R. S. 1981. The myocardium as a fluid-fiber continuum: passive equilibrium configurations, 1981 Advances in Bioengineering. American Society of Mechanical Engineers. New York. 135–138.

Feit, T. S. 1979. Diastolic pressure-volume relations and distribution of pressure and fiber extension across the wall of a model left ventricle. *Biophys. J.* 28:143–166.

Fox, C. C., and G. M. Hutchins. 1972. The architecture of the human ventricular myocardium. *Johns Hopkins Med. J.* 130:289–299.

Mirsky, I. 1979. Elastic properties of the myocardium: a quantitative approach and clinical applications. *In* Handbook of Physiology, Vol. 1. R. M. Berne, N. Sperelakis, and S. R. Geiger, editors. American Physiological Society, Bethesda, Maryland. Section 2.

Moskowitz, S. E. 1981. Effects of inertia and viscoelasticity in late rapid filling of the left ventricle. *J. Biomech.* 14:443–445.

Peskin, C. S. 1975. Mathematical Aspects of Heart Physiology. Courant Institute of Mathematical Sciences, New York.

Pierce, W. H. 1981. Body forces and pressures in elastic models of the myocardium. *Biophys. J.* 34:35–59.

Rankin, J. S., P. A. McHale, C. E. Arentzen, D. Ling, J. C. Greenfield, R. W. Andersen. 1976. The three-dimensional dynamic geometry of the left ventricle in the conscious dog. *Circ. Res.* 39:304–313.

Sagawa, K. 1978. The pressure-volume diagram revisited. *Circ. Res.* 43:677–687.

Streeter, D. D. 1979. Gross morphology and fiber geometry of the heart. *In* Handbook of Physiology, Vol. 1. R. M. Berne, N. Sperelakis, and S. R. Geiger, editors. American Physiological Society, Bethesda, Maryland. Section 2.

Yoran, C., J. W. Covell, and J. Ross. 1973. Structural basis for the ascending limb of left ventricular function. *Circ. Res.* 32:297–303.